

Overcoming the Force Limitations of Magnetic Robotic Surgery: Magnetic Pulse Actuated Collisions for Tissue-Penetrating-Needle for Tetherless Interventions

Onder Erin,* Xiaolong Liu, Jiawei Ge, Justin Opfermann, Yotam Barnoy, Lamar O. Mair, Jin U. Kang, William Gensheimer, Irving N. Weinberg, Yancy Diaz-Mercado, and Axel Krieger*

The field of magnetic robotics aims to obviate physical connections between the actuators and end-effectors. Such tetherless control may enable new ultraminimally invasive surgical manipulations in clinical settings. While wireless actuation offers advantages in medical applications, the challenge of providing sufficient force to magnetic needles for tissue penetration remains a barrier to practical application. Applying sufficient force for tissue penetration is required for tasks such as biopsy, suturing, cutting, drug delivery, and accessing deep-seated regions of complex structures in organs such as the eye. To expand the force landscape for such magnetic surgical tools, an impact force-based suture needle capable of penetrating *in vitro* and *ex vivo* samples with 3-degrees-of-freedom (DOF) planar motion is proposed. Using custom-built 14 and 25 G needles, generation of 410 mN penetration force is demonstrated, a 22.7-fold force increase with more than 20 times smaller volume compared with similar magnetically guided needles. With the Magnetic Pulse Actuated Collisions for Tissue-penetrating (MPACT)-Needle, gauze mesh suturing onto an agar gel is demonstrated. In addition, the tip size is reduced to 25 G, a typical needle size for eye interventions, to demonstrate *ex vivo* penetration in a rabbit eye towards corneal injections and transscleral drug delivery.


1. Introduction

State-of-the-art surgical robots (e.g., da Vinci Surgical System^[1]) enable minimally invasive procedures by providing surgeons with finer control and increased mobility via a few small incisions. However, these robotic manipulators have large mechanical footprints in the patient compared with surgical end-effectors (e.g., needles and grippers), making the robotic manipulator the most invasive component involved in the procedure. Magnetically guided robotic systems have the potential to revolutionize surgical interventions by allowing tetherless access to magnetic tools operating inside the body. Using such a paradigm, magnetic fields could wirelessly guide magnetic agents (i.e., end-effectors) accurately and safely, obviating the mechanical manipulator and paving the way for untethered robotic surgical systems.^[2-6] Such a system may enable ultraminimally invasive procedures, like the closing of a hole in the heart or repairing a hernia via insertion of

only a needle and suture thread, as opposed to insertion of multiple trocars for manipulation of a needle and suture thread.

O. Erin, X. Liu, J. Ge, J. Opfermann, A. Krieger
Department of Mechanical Engineering
Johns Hopkins University
Baltimore, MD 21218, USA
E-mail: oerin@jhu.edu; axel@jhu.edu

Y. Barnoy
Department of Computer Science
Johns Hopkins University
Baltimore, MD 21218, USA

 The ORCID identification number(s) for the author(s) of this article can be found under <https://doi.org/10.1002/aisy.202200072>.

© 2022 The Authors. Advanced Intelligent Systems published by Wiley-VCH GmbH. This is an open access article under the terms of the Creative Commons Attribution License, which permits use, distribution and reproduction in any medium, provided the original work is properly cited.

DOI: 10.1002/aisy.202200072

L. O. Mair, I. N. Weinberg
Weinberg Medical Physics, Inc.
North Bethesda, MD 20852, USA

J. U. Kang
Department of Electrical and Computer Engineering
Johns Hopkins University
Baltimore, MD 21218, USA

W. Gensheimer
Department of Ophthalmology
Dartmouth-Hitchcock Medical Center
Lebanon, NH 03756, USA

Y. Diaz-Mercado
Department of Mechanical Engineering
University of Maryland
College Park, MD 20742, USA

The size of a surgical tool or end-effector plays a crucial role in determining how minimally invasive a surgery could be.^[7–11] Magnetically guided end-effectors can be very small, as they are manipulated without contact and have no requirement to carry on-board power supplies or other electronics.^[12–15] However, magnetic pulling forces scale with L^3 (L is the characteristic length of the magnetic object), while resistive forces such as drag forces scale with L^2 . As such, magnetic pulling forces are not dominant for small devices. Clinically relevant applications that include tissue penetration, biopsy, or suturing become either technically demanding or infeasible at such scales. Required forces can be achieved by bringing magnets very close to the end-effector^[16,17] or increasing the power of electromagnets using greater coil currents. However, medical applications impose boundaries on how close external magnets can approach end-effectors for clinical usefulness, and large currents in electromagnets create difficulties due to resistive losses and heating.^[18,19] Thus, innovative methods of generating large end-effector force while maintaining tetherless operation have the potential to expand the magnetic surgery toolbox.

Magnetically actuated biopsy procedures have been demonstrated in vitro and ex vivo.^[16,20] Due to the high force requirements of these systems, unorthodox robot design methodologies have been developed. Vartholomeos et al. demonstrated a grounded gear train that is powered by the magnetic pulling forces generated inside a magnetic resonance imaging (MRI) scanner.^[21] The grounded robotic system has dimensions $10 \times 10 \times 6$ cm and is located outside of the patient. The biopsy needle can be pushed and pulled along a single desired direction in 3D space. To meet the high force requirements, this system uses a lever arm and a rotational mechanism connected to a gear train mechanism that results in a translational motion of the needle tip. As an alternative approach, untethered magnetic capsule-based biopsy operations can be performed only in the near vicinity of the electromagnetic actuators due to the high force requirements.^[16] However, methods for applying sufficient linear forces to clinical-scale needles so as to enable tissue penetration or the basic functions of biopsy are still needed to advance the field. An alternative material engineering approach is demonstrated by Li et al. to provide high force outputs. The soft magnetic muscle material has been shown to respond to radiofrequency (RF) heating and shrinks its size when the temperature is high.^[22] Such a shrink in size has been shown to provide high force delivery for drilling, suture, and cutting applications. Permanent magnet-based systems are developed to provide stronger forces. A set of magnets that consists of a small bore similar to Hallbach and Aubert arrays have shown the potential to exert stronger magnetic forces and torques.^[23,24] So far, these systems require the workspace to move (rotate and translate) inside the magnetic bore for dexterous steering of magnetic robots. Moving the patient's bed continuously to accomplish complex navigation tasks could be a practical concern for medical operations, where the patient's bed should remain still. In contrast, electromagnetic actuation systems do not have such a concern. However, many electromagnetic systems are unable to provide sufficient force due to the limitations in electrical power. Therefore, a complete penetration from outside of the sample with large penetration distances remains as a challenge for millisized-miniature magnetic needles, as shown in our previous study.^[25]

Recent studies have demonstrated the advantage of using magnetic impulse impacts to generate large instantaneous forces that suffice for various tissue penetration applications.^[26–28] The fundamental enabling principle in these studies is to magnetically slide a magnetic element inside of a larger container, allowing the magnetic element to gain sufficient velocity such that, upon striking an impact plate on one side of the container, the impact transfers the sliding magnet's momentum to the impact plate, inducing a momentary force on the entire device or at the needle tip. This technique has been used by Becker et al. to create an MRI-powered multimodule Gauss gun.^[26] Once the robots get close enough to each other beyond the critical distance, the magnetic mechanism is triggered and a magnetic bead starts to accelerate and strikes a mobile needle tip. The momentum transfer onto the needle tip creates a projectile motion and the needle tip can go deep in the tissues. Quelin et al. used a similar impact method to create 2D locomotion of a microrobot prototype that is impact driven.^[28] This system allows fine positioning of the chip with relatively smaller magnetic forces. Similarly, Leclerc et al. demonstrated the use of such an impact force by developing a monodirectional magnetic hammer in which a 6 mm-diameter sphere magnet is pulled and pushed inside a hollow tube, enabling penetration into the ex vivo lamb brain.^[27]

However, these systems do not provide the degrees-of-freedom (DOF) motion capability that is required by most penetration applications for needle steering. For example, due to the strong and constant main magnetic field of an MRI device,^[29] the aforementioned Gauss gun and the MRI-powered hammer can penetrate only along a single direction. A full planar DOF is required for complete operation beyond straight-line motion. In addition, considering the centimeter-scale dimensions of these devices and their inability to orient to any desired penetration angle, such designs could be used only for biopsy along a single axis toward a single direction but could not be used for minimally invasive suturing applications that require 3-DOF or interventions in the eye with ≈ 25 G-sized needle tip. Similarly, precise positioning of 25 G needles is essential for clinical tasks such as hydrodissection and controlled intraocular access in cornea surgeries. During a cornea transplant, the surgeon must penetrate the eye, passing a needle up to 90% of way through the cornea thickness for best patient outcomes.^[30] Robots for autonomous cornea penetration are either too heavy to be eye mountable or are too slow for clinical use.^[31] Magnetically induced cornea penetration for intraocular access with a 25 G needle may be one solution for robot-assisted cornea surgeries as a lightweight and effective penetration solution.

Here we present the design and evaluation of a Magnetic Pulse Actuated Collisions for Tissue-penetrating Needle (MPACT-Needle) to close the gap to achieving relevant levels of forces for magnetic needles and other magnetic miniature tools. This custom-built magnetic needle design brings the size-to-force trade-off into more favorable levels for medical applications. The internal impact mechanism of the MPACT-Needle provides stronger penetration forces at small, clinically relevant size scales. For our MPACT-Needle, the impact mechanism yields 22.7-fold higher penetration forces at the moment of impact. In addition, we decrease the size of these impact-based devices by more than a factor of 20, and therefore, the volumetric footprint and weight of these devices are significantly reduced.^[28]

Moreover, we demonstrate multi-DOF planar steering and manipulation (X- and Y-axis translation and in-plane rotation) instead of a single DOF mechanism.^[27] Therefore, the MPACT-Needle design results in an efficient use of electromagnetic systems, which have limits on power exertion, by transmitting the same magnetic energy into much stronger and efficient impact forces, thanks to the sliding magnetic piston design.

We use our MPACT-Needle end-effector to demonstrate multiple surgically relevant tasks such as in vitro suturing and ex vivo eye cornea penetration for tissue hydrodissection and minimally invasive access. The requirements of a suturing task are typically prescribed by the sewing motion of the needle, requiring the needle to rotate and penetrate in various directions or at various angles, a capability we demonstrate here. Expanding on previous studies, we demonstrate 3-DOF steering of a needle that is oriented by torque-inducing magnetic fields and directed with magnetic gradient fields. This needle then operates in the impact-momentum exertion mode via rapidly switching magnetic field gradients.

Conceptual depiction and the principal mechanism of the MPACT-Needle is demonstrated in **Figure 1**. Magnetic suturing tasks and eye cornea penetration for tissue hydrodissection and minimally invasive access (demonstrated in Figure 1a) are our primary clinically relevant applications for the MPACT-Needle. We utilize the electromagnetic system and the novel MPACT-Needle design to accomplish these tasks, as depicted in

Figure 1b,c. In addition, we present a design optimization and experimental validation that maximizes the impact force generated at the needle tip and guides the selection of the magnetic piston length and the shaft length. We also present a scaling analysis for the needle dimensions (diameter and length) to show how the impact forces scale using mathematical computations and experimental measurements with various MPACT-Needle sizes. Along with the scaling analysis, an electrical power-scaling analysis is also conducted to demonstrate the range of electrical power required for generating magnetic fields capable of various ex vivo and in vivo suturing experiments. Using our optimized design, we demonstrate a running suture implementation with in vitro agarose gel samples to move the MPACT-Needle concept closer to clinically relevant suturing tasks. Moreover, we present our ex vivo results on transcorneal penetration with a 25 G needle tip to demonstrate the capacity in clinically relevant tasks.

2. Results

2.1. MPACT-Needle Design, Manufacturing, and Optimization

2.1.1. Needle Design and Manufacturing

The MPACT-Needle embodies the features of a suturing needle while incorporating a dynamically moving magnetic piston

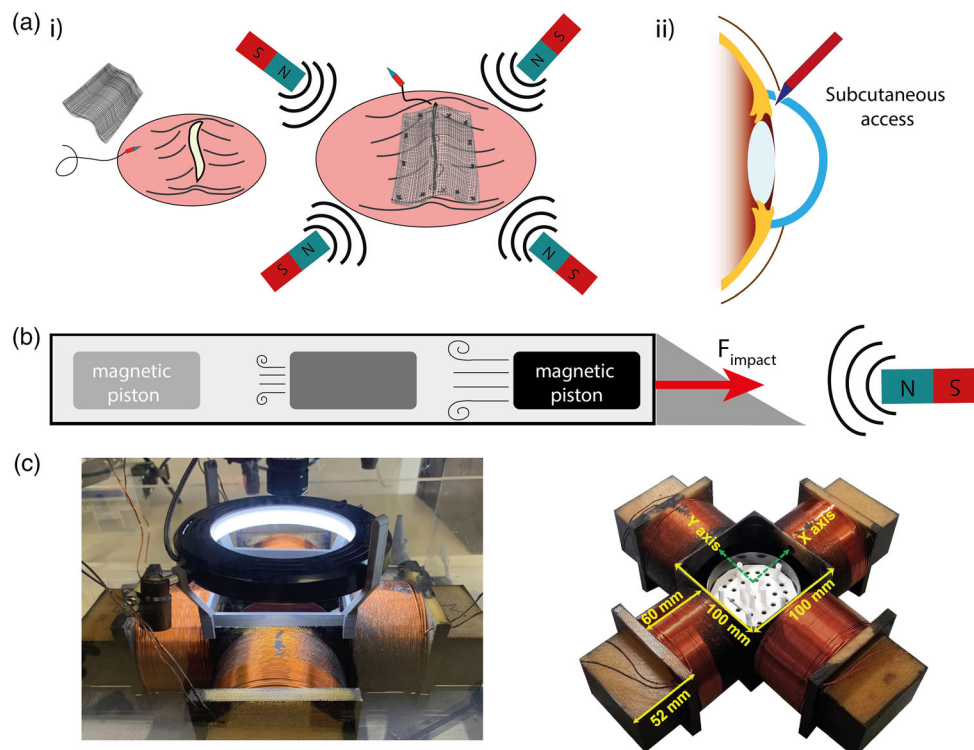


Figure 1. Magnetic suturing and tissue penetration with the benefit of impact forces. a.i) A typical procedure for hernia repair is to use a mesh and a suturing needle to close a defect. A magnetic needle controlled by external magnetic fields could accomplish this procedure remotely by revolutionizing the surgery with an ultra minimally invasive, magnetically controlled suture needle approach. a.ii) Tissue access, that is, cornea access to eye, requires strong penetration forces from a needle. The proposed magnetic device could be able to provide transcorneal or transscleral access for various medical procedures. b) To overcome the force limitation for miniature magnetic robots, we designed and manufactured MPACT-Needle which utilizes a moving magnetic piston's momentum to realize momentarily high force outputs for tissue penetration. c) The running suture path to stitch a mesh into an agar gel and eye penetration is accomplished by the four-electromagnetic coil system.

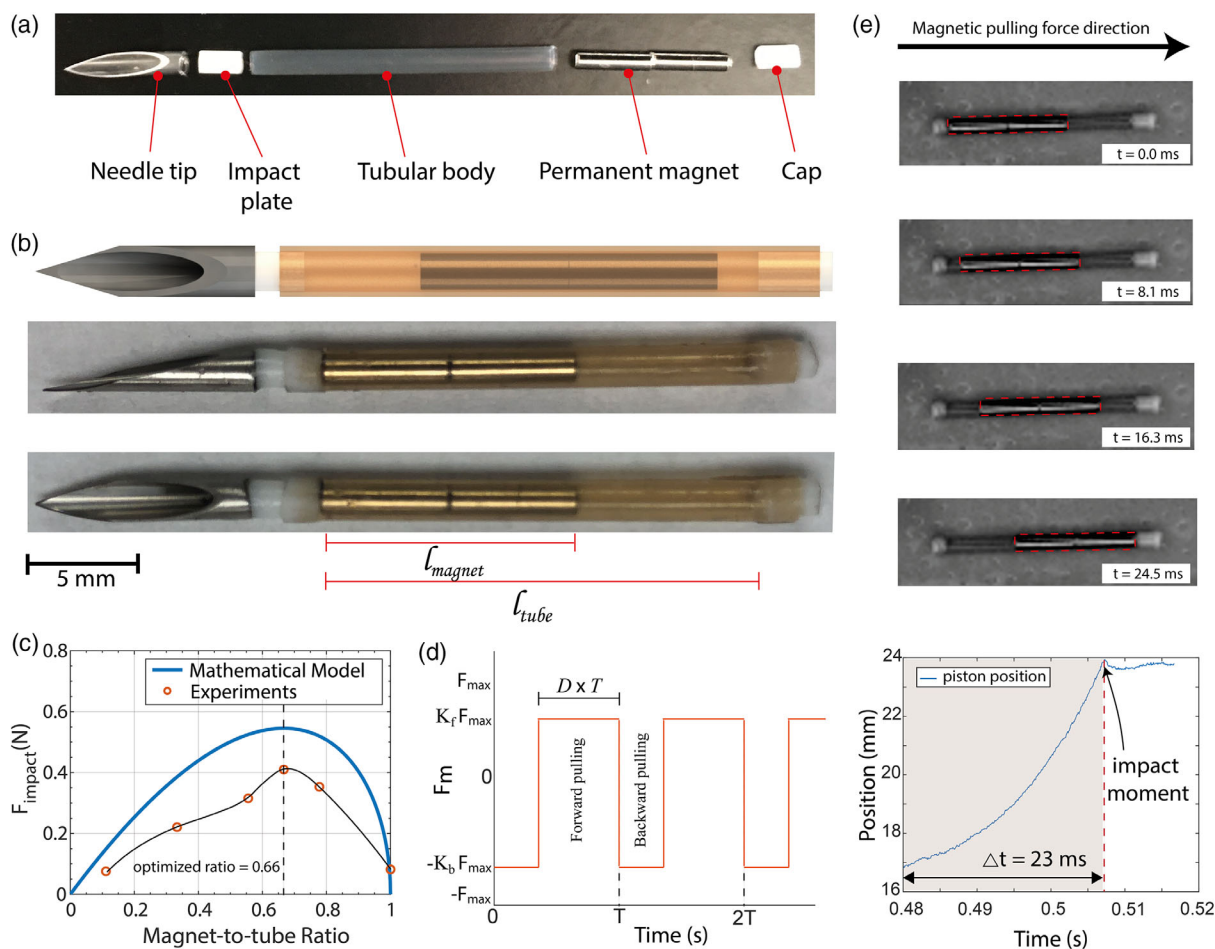


Figure 2. Impact-based needle design, impact mechanism with magnetic actuation sequence, and magnet length optimization. a) The impact-based magnetic needle consists of five main components: the needle tip, impact plate, tubular body, permanent magnet, and a cap. b) These components are assembled via cyanoacrylate-based adhesives or press-fit inside the tubular structure. The permanent magnet is slightly smaller than the diameter of the tubular structure and is sized so as to allow it to freely move back and forth within the tube. c) Increasing the length of the magnet increases the applied magnetic force but reduces the possible travelling distance within a limited tubular body. To maximize the impact force, the optimum size of the magnet is found to be 0.66 times of the overall tubular body length. d) The motile magnet is being pulled back and forth in the tubular body to create repetitive impact forces. The magnetic field created keeps the alignment of the magnet along the penetration direction. e) High-speed recording snapshots of the collision moment and the overall magnet stroke.

inside the needle's shaft. This MPACT-Needle design, optimization, and actuation sequence with impact mechanism are presented in **Figure 2**. The MPACT-Needle, shown in **Figure 2a,b**, comprises five components: 1) a needle tip; 2) a tubular body; 3) a permanent magnet; 4) an impact plate; and 5) a cap. To provide strong forces and the ability to suture while keeping the footprint small, we selected a 14 G needle diameter as a compromise among needle manufacturability, medical relevance, and attainable force. Needing only the sharpened hypodermic needle tip, we cut 9 mm from the tip of a standard tribeveled standard hypodermic needle (14 G puncture needle, TC INC). For suturing application, the needle tip size used is 14 G; for eye penetration, we used a 25 G hypodermic needle tip. The permanent magnet is a NdFeB magnet (Cyl0050, Supermagnetman) that has a cylindrical shape of 1.5 mm diameter and 12.1 mm length. These magnets are inserted into the MPACT-Needle's tubular body, which is made of polytetrafluoroethylene (PTFE) plastic

(75175A671, McMaster-Carr) that is 18.4 mm long with an outer diameter of 2.08 mm and inner diameter of 1.67 mm. The impact plate and cap were composed of a glass-mica (Macor) cylindrical rod composite (8489K11, McMaster-Carr), both having identical dimensions of 3 mm length and 1.6 mm diameter. The magnet diameter is selected as slightly smaller than the tube's inner diameter to maximize the magnetic force (NdFeB volume) while still allowing ample space for the magnet to accelerate in the hollow shaft, as well as ample clearance for the magnet to slide smoothly along the interior of the needle shaft. The impact plate is designed to efficiently deliver the impact force from the magnet to the needle tip, ideally with as little force loss as possible. Therefore, a Macor ceramic was chosen for its stiffness, impact resistance, and machinability. Moreover, since glass-mica ceramic is a nonconductive material, the potential eddy current generation and the resulting magnetic breaking phenomena are avoided. Both the impact plate and cap are

assembled via a press fit to the plastic tubular body. The needle tip is attached to the impact plate using a cyanoacrylate-based adhesive. A similar adhesive is used for attaching the suture thread at the tail of the needle.

2.1.2. Magnetic Piston Design Optimization

Maximizing the impact force while minimizing the length of the needle shaft is the main goal of the design optimization. Increasing the length of the magnet increases the magnetic pulling force, F_m , and the magnet mass, m . However, the travelling distance from tail to the tip of the needle decreases, allowing less distance for build-up of momentum. While a larger mass indicates a stronger impact momentum, shorter travelling distances result in smaller velocity magnitudes and weaker impact momentum. Therefore, there is an optimum ratio between the length of the magnetic piston and the tube length to maximize the impact force. Therefore, the optimization problem can be defined as

$$\begin{aligned} & \underset{l_{\text{magnet}}}{\text{maximize}} && f_{\text{impact}}(l_{\text{magnet}}) \\ & \text{subject to} && l_{\text{magnet}} \leq l_{\text{tube}} \end{aligned} \quad (1)$$

where $f_{\text{impact}}(l_{\text{magnet}})$ is the objective function, l_{magnet} is the length of the magnet, and l_{tube} is the length of the tube. Defining $k = l_{\text{tube}} - l_{\text{magnet}}$ as the travelling length of a magnet from the tail to the tip of the needle and considering Equation (6), (7), and (8), the impact momentum under a constant acceleration toward the tip can be defined as $l_{\text{magnet}}\sqrt{2ak}$. To maximize the impact force, this impact momentum should be maximized. Defining constants under a single constant parameter, $C = \rho_m \pi r_m^2 \sqrt{2a}$, yields the objective momentum function as $Cl_{\text{magnet}}\sqrt{k}$. Replacing $k = l_{\text{tube}} - l_{\text{magnet}}$ yields the optimization function as

$$\underset{l_{\text{magnet}}}{\text{maximize}} \quad f(l_{\text{magnet}}) = Cl_{\text{magnet}}\sqrt{(l_{\text{tube}} - l_{\text{magnet}})} \quad (2)$$

Equilibrium $\frac{df(l_{\text{magnet}})}{dl_{\text{magnet}}} = 0$ yields the optimum final relation as

$$l_{\text{magnet}} = \frac{2l_{\text{tube}}}{3} = 0.66l_{\text{tube}} \quad (3)$$

By setting $l_{\text{tube}} = 18.4$ mm for the needle proposed in this study, the optimum l_{magnet} was found to be 12.1 mm.

We have experimentally and mathematically swept the magnet-to-tube ratio, as shown in Figure 2c, and pinpointed the optimized ratio as 0.66 experimentally as well. For experimental testing, various MPACT-Needles with different l_{magnet} sizes are manufactured by sweeping the l_{magnet} parameter from 2 to 18 mm while keeping the l_{tube} constant at 18.4 mm. As shown in Figure 2c, a nonoptimized design could result in a significant reduction of the maximum impact force accomplishable by the needle, making the penetration infeasible. For the range of experimental measurements, we found out that a nonoptimum magnetic piston length selection may result in a factor of 9.7 less impact force than the optimized version. The equivalent impact force is the summation of the pulling force and momentum

transfer-based force. The magnetic pulling force and manufacturing errors (submillimeter gaps in the tube for the magnet to travel) result in nonzero impact force results for the unity magnet-to-tube ratio case.

2.2. Impact Mechanism and Time-Dependent Parameters

The cylindrical permanent magnet can freely move inside the tubular body back and forth. The magnetic field is sequentially generated to pull and push this magnetic piston inside the tube while preserving the magnetic alignment. Forward pushing results in collision of the magnetic piston with the ceramic impact plate. This collision generates a sudden impact force at the moment of the impact. Amount of this force is much stronger than the force that can be accomplished by pure magnetic pulling. Therefore, needle penetration requiring tasks with miniaturized tool sizes becomes possible for magnetic robotics. Figure 2d defines this alternating pushing and pulling actuation sequence. The performance of the overall impact force depends on the period of the sequence, T , duty ratio of the forward motion, D , as well as forward and backward pulling force constants, K_f and K_b , respectively. To maximize the impact force, the strongest pulling force should be applied (i.e., $K_f = 1$), and the NdFeB magnet should travel the longest possible distance. That is, ideally, the magnet starts at the tail of the shaft and travels the entire distance along the tube, striking the impact plate and remaining in contact with the impact plate until all magnet momentum is transferred. Hence, the selection of both D and T determines the impact force performance. Improper selection of parameters D and T will result in incomplete or inefficient transfer of force from the magnet to the impact plate. This could happen either because the magnet does not transfer momentum completely or because the magnet does not reach the impact plate due to premature stopping. Similarly, the backward force must also be tuned properly such that the magnet travels backward, recovering the travelling distance for subsequent, cyclic impact events without causing a considerable backward impact force.

To visualize the impact moment, the needle tube is attached on top of a double-sided tape and a high speed camera (Photron, FASTCAM SA5, San Diego, CA, USA) is mounted on top of the workspace. Figure 2e demonstrates the high-speed camera snapshots of the impact moment as well as the piston position tracking for this specific stroke. The magnet travels from one end to the other end in 23 ms, transfers the momentum, and shows a slight bounce back as the tube is rigidly attached to the double-sided tape.

2.3. Impact Force Characterization and Scaling of the Robotic System

2.3.1. Characterization of Pulsing Sequence

We have experimentally measured the impact force by sweeping D and T to find the optimal actuation configuration to maximize the net force. We swept D from 0.2 to 0.8 with 0.1 increments. Similarly, we swept T from 0.05 to 0.25 s in 0.05 s of increments. **Figure 3** presents the experimental measurement system, results

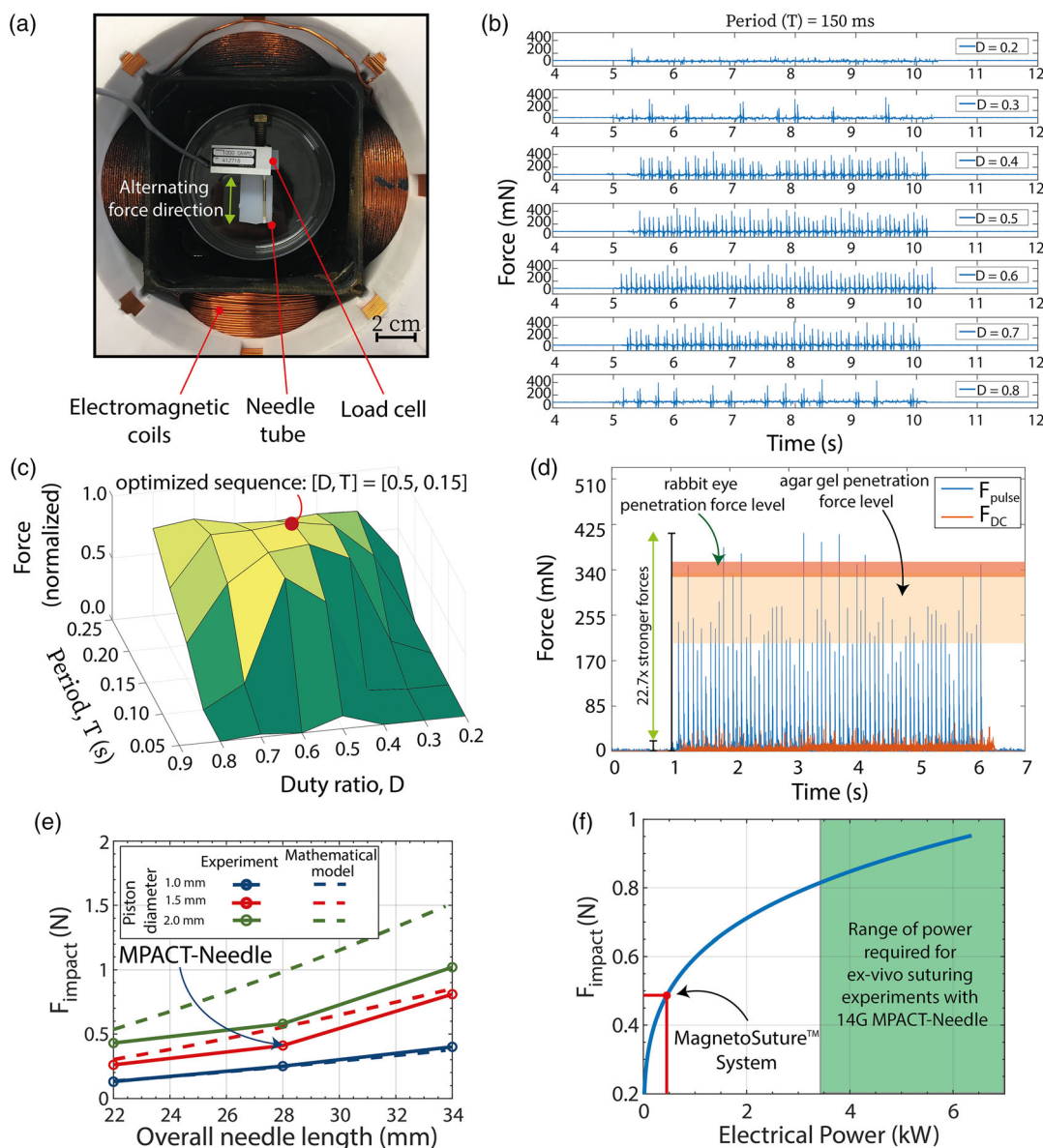


Figure 3. Characterization experiments and scaling analysis. a) The forces are measured using a load cell under the workspace of the electromagnetic coil system. b) For a selected well-performing period duration, $T = 150$ ms, the impact force measurements with respect to time are shown. The duty ratio, D , values ranging from 0.2 to 0.8 is swept with 0.1 increments. Having D in the range of 0.4–0.6 yields more than 400 mN momentarily forces in the needle. c) Selection of impractical D and T values results in degradation of the force performance. The optimal value for D and T is found to be 0.5 and 0.15 s for this study. d) Compared with the DC pulling force, the impact-based mechanism provides 22.7 times higher forces to allow penetration into tissue. e) Scaling of the needle dimensions is analyzed by manufacturing and experimentally measuring the impact force of each size of needle. The diameter and needle length are the two important factors in scaling. Larger the needle, the more impact force we can acquire. f) Higher electrical power levels on the electromagnetic coils allow exerting stronger impact forces. MagnetoSuture System results in more than 400 mN forces for optimized miniature needle dimensions at 14 G.

of the experiments, as well as theoretical scaling analysis for the needle and the system. For the experiments, we used a load cell (Transducer Techniques, GSO-1K) and located the tube at the center of the workspace, as shown in Figure 3a. We applied the pulsing sequence by having a 2D sweep for D and T variables while recording the measured force in real time. Experimental results (Figure 3b,c) indicate that, for the highest and the most repetitive impact mechanism, the ideal period of the sequence, T ,

was found to be 0.15 s, while the ideal duty ratio D was 0.5 when the needle was at the center of the workspace.

It should be noted that T varies depending on the needle location inside the Petri dish due to the nonhomogeneous magnetic gradient distribution. For the cases when the needle is far from the center, the user could manually tune K_f and K_b constants to ensure proper operation of the impact mechanism. Reducing the forces with K_f and K_b would result in larger T values depending

on the deviation from the center. We used these experimentally acquired optimization values for T and D for force comparison between typical magnetic pulling forces and impact forces of MPACT-Needle. We measured both the pulsing impact force and DC gradient pulling force to determine force values, each measurement being performed three times. The acquired data were used to compare the impact-based penetration force with the typical magnetic pulling force without any impact for the same needle. To acquire the DC pulling force for our design, we applied and measured the DC pulling force when the magnetic piston is in contact with the impact plate already. The same setup and the same magnetic device were used for measuring the impact forces for the optimized actuation sequence. Both DC force measurements and impact force measurements with respect to time are provided in Figure 3d to provide better contrast with the force amplification accomplished with the impact force mechanism. As the DC pulling force should be constant under a constant pulling force, the DC pulling force is determined by taking the mean of the accumulated data over 6 s. On the other hand, as the impact force is a momentary burst of force, we took the mean of the highest peaks of three strokes to demonstrate an achievable magnetic force. This comparison has shown that, while the impact-force based mechanism can provide up to 410 mN of force for the optimal magnet-to-tube ratio (0.66), the continuous gradient pulling force mechanism can only provide 18 mN of force at the center of the workspace (Figure 3d). According to the microscopy (UM1000, AMScope) image measurements, we found that the needle tip is 0.11 mm thick and 0.032 mm wide, resulting in a tip area of 0.0035 mm². This would result in 117 MPa pressure applied at the very needle tip at each impact applied.

2.3.2. Needle-Size Scaling

To understand the trend and expected impact force values as a function of needle diameter and length, we calculated the impact force on the needle for various dimensions of the tube geometry. While maintaining the optimized magnet-to-tube ratio constant (described in the Design Optimization subsection under Experimental Section), we scaled the needle length and the needle diameter. The magnetic piston length and its diameter are scaled along with the dimensions of the needle. The impact force, f_{impact} , is calculated with the assumption of perfect momentum transfer, which is a reasonable approach as we use Macor impact plate rather than a soft plastic material. The impact force is assumed to be constant over the duration of the impact, Δt_{impact} , which is experimentally measured as 400 μs with a load sensor. As the friction force on the magnetic piston is orders of magnitude smaller than the magnetic pulling force, we neglect the effect of friction force. With the constant acceleration of the piston before the impact with the magnetic pulling force, F_m , the resultant impact force, f_{impact} , can be calculated as

$$f_{\text{impact}} = m \sqrt{\frac{2 F_m k}{m}} \Delta t_{\text{impact}} \quad (4)$$

where k is the net distance the piston can travel: $k = l_{\text{tube}} - l_{\text{magnet}}$. F_m , m , and k depend on the needle-size scaling and each of these

terms scales as L^3 , L^3 , and L , respectively (further details are provided in Experimental Section). Thus, according to Equation (4), the overall scaling law of the impact force is found to be proportional to $L^{3.5}$. This indicates that the impact force mechanism is preferable at larger scales and may require more magnetic power or adapting the electromagnetic setup size for smaller scales. The trend can also be seen in Figure 3e.

To complement the theoretical findings with experiments, we manufactured various sizes of MPACT-Needle bodies to experimentally explore the relationship between needle size, length, and impact force. While keeping the optimized magnet-to-tube length ratio constant, we used 8, 12, and 16 mm as the magnetic piston lengths and 1.0, 1.5, and 2.0 mm as the diameters of the magnetic pistons, resulting in a total of nine different MPACT-Needle geometries. The experimental results of the scaling analysis show a similar trend with the mathematical model of Equation (4) with some intensity mismatch between the experimental measurements and mathematical estimations (Figure 3e). The error in experimental measurements is derived from multiple sources, including variations in friction between the piston and the inner tube, slight sample positioning mismatches, magnetic field modeling inaccuracy, and custom-made needle manufacturing errors. Assumptions in the mathematical model such as perfect momentum transfer and constant impact force during the impact event are also potential contributors to the discrepancies between experimental measurements and the mathematical model.

2.3.3. Electrical Power Scaling

Our electromagnetic coil system can exert a finite force limited by the power train, motor controllers, and coil geometry. Based on the mathematical model shown in Equation (4), we estimated the impact force with respect to the power applied on the electromagnetic coils (Figure 3f). The result shown in Figure 3f indicates a nonlinear relation between the electrical power and the impact force. In our experimental measurements and trials for the penetration of a bacon strip, chicken tissue, and rabbit abdominal wall (Supplementary Information), the penetration force requirements suggest that for the current MagnetoSuture System, more than 7.5 times the available electrical power is required for a magnet at the center of the workspace (approximately at a distance of 5 cm from the electromagnetic coil surface to the center of the needle magnet). Even though the power and the impact force do not scale linearly, 3.5 kW or more electrical power would bring the penetration of the MPACT-Needle into the force range for ex vivo suturing applications.

2.4. In Vitro Suturing and ex vivo Eye Penetration with MPACT-Needles

Using the MPACT-Needle and associated optimized controlling parameters T and D , we aimed to demonstrate how the significant force increase enabled the completion of challenging tissue penetration tasks. Due to the scaling laws for magnetic actuation, it is challenging to achieve sufficient force for penetration with a miniature needle using gradient pulling methods. We experimentally characterized the required penetration forces for five

different types of samples. These samples are rabbit abdominal wall, chicken breast tissue, rabbit eye, 0.6% Agar gel, and bacon strip. We repeated each penetration experiment at least five times. Our experimental findings regarding the required penetration forces are summarized in **Table 1** and further information about the measurement setup and acquired data is provided in the Supplementary Document. For the suturing and transcorneal penetrations, the MPACT-Needle provides sufficient penetration forces. On the contrary, suturing onto rabbit abdominal wall, chicken tissue, or bacon strip would require a stronger electromagnetic coil system, as shown in the table. To demonstrate the basic suturing capabilities and eye cornea access, we demonstrate 1) *in vitro* suturing of tissue phantoms with a mesh and 2) *ex vivo* rabbit eye penetration in two different experiments. In the first experiment, we implemented a suturing task, stitching a gauze mesh on an agarose gel tissue phantom, the objective being a procedure that mimics a hernia repair surgery. We prepared 0.6% agarose gel with 3 mm thickness and then covered one surface of the agarose gel with a gauze mesh.^[32] This sample was clamped vertically and placed along the centerline of the workspace. This centered clamp configuration allows us to steer the needle freely to demonstrate suturing tasks within the workspace of our magnetic system. It is important to note that the penetration forces at the start of penetration were lower as the location of the magnetic piston was at the far end of the attractive coil to penetrate. The back-and-forth hammering motion is partially automated. This partial automation takes the handheld remote controller (Xbox Controller, VOYEE) input and maps this into a hammering behavior on the magnet. By changing the polarity and current intensity of the electromagnets, we can keep the alignment of the magnet pointing toward the direction of penetration while moving the magnetic piston back and forth, with the user tuning the intensity of the backward pulling force. Both positional and orientational steering are performed manually using the handheld remote controller which controls the coils via pulse width modulation signals sent from a motor controller to the MagnetoSuture coils. The MPACT-Needle was able to generate more than 248 mN penetration force in average, which is found to be the penetration force required for the agarose gel used in this study. The applied running suture, consisting of three penetrations, was completed in 158 s. Agarose gel and mesh suturing results are presented in **Figure 4**.

In the second experiment, a 25 G MPACT-Needle was combined with a trephine to demonstrate full-thickness cornea tissue

penetration using the MagnetoSuture System as a first step toward tissue hydrodissection and minimally invasive intraocular access in ocular surgery (**Figure 5a**). A whole rabbit eye was prepared by dissecting the conjunctiva and injecting phosphate-buffered saline to achieve an intraocular pressure of 20 mmHg. The eye was placed in line with the coil axes of the MagnetoSuture system and trephine was secured using a clinical vacuum system (Moria Surgical, 17202D800). It is important to note that trephine was positioned such the 25 G MPACT-Needle was aligned with the coil axis to maximize the thrust of the needle (**Figure 5b**). The eye was angled 30° with respect to the needle to replicate the setup used in the force characterization tests. Using a partially automated hammering strategy, the MagnetoSuture System achieved full thickness corneal penetration in 30.1 s (**Figure 5c**) and achieved a thrust force in excess of 364.9 mN based on rabbit cornea tissue characterization tests described in the methods. After tissue penetration, the vacuum pressure was released and the trephine with MPACT-Needle was removed from the rabbit eye. Visual inspection of the cornea revealed an acute defect at the site of needle penetration, as highlighted in **Figure 5d**. Once the rabbit eye was removed from the MagnetoSuture System, the corneal tissue collapsed, indicating loss of intraocular pressure consistent with a needle puncture.

3. Discussion

One of the key challenges in magnetically actuated robotics is overcoming the problems of insufficient force imposed by the scaling laws of applied magnetic forces on small robotic end-effectors or devices. Miniature robots either require special designs for true penetration into a tissue, or they require very high electrical power and short distances to electromagnets that are incompatible with clinically relevant applications. While we were accomplishing up to 30 mN force using a sharpened NdFeB needle with the same electromagnetic system in our previous work,^[33] and 18 mN by only continuous magnetic gradient pulling of the MPACT-Needle, with the MPACT-Needle optimized design and actuation mechanism, we are able to accomplish up to 410 mN momentary penetration force. This mechanism and actuation technique proposed can be implemented in any other magnetic needle or magnetic tool to increase actuation forces.

In this work, we demonstrate impact force-based penetration that can significantly enhance the penetration force (22.7-fold improvement), allowing the needles to penetrate into rabbit cornea and tissue-like gels successfully. Rabbit corneas were chosen for these experiments because they exhibit similar mechanical properties to human tissue, and human cadaveric eyes were not available for testing. When accounting for needle gauge and bevel angle, the forces required to penetrate human cornea and corneoscleral limbus tissues are 282 and 382 mN, respectively.^[34,35] These forces are similar to the penetration force we experimentally derived for rabbit tissues (364.9 mN), demonstrating that the MagnetoSuture system is capable of clinical corneal penetration and intravitreal injections. This mechanism offers an important potential route of force magnification for suturing and other needle-based interventions in clinically relevant settings, where repetitive mechanical penetration is required.

Table 1. Experimentally measured penetration forces for hypodermic needles in various types of samples.

Penetration force Measurements	Sample				
	Type				
	Rabbit Abdominal Wall	Chicken Breast Tissue	Rabbit Eye	Bacon Strip	Agar Gel (0.6%)
Needle size [C]	14	14	25	14	14
Mean force [N]	0.85	0.55	0.36	0.46	0.25
Std force [N]	0.25	0.23	0.06	0.11	0.01
Experiment repetition [n]	8	8	5	5	8

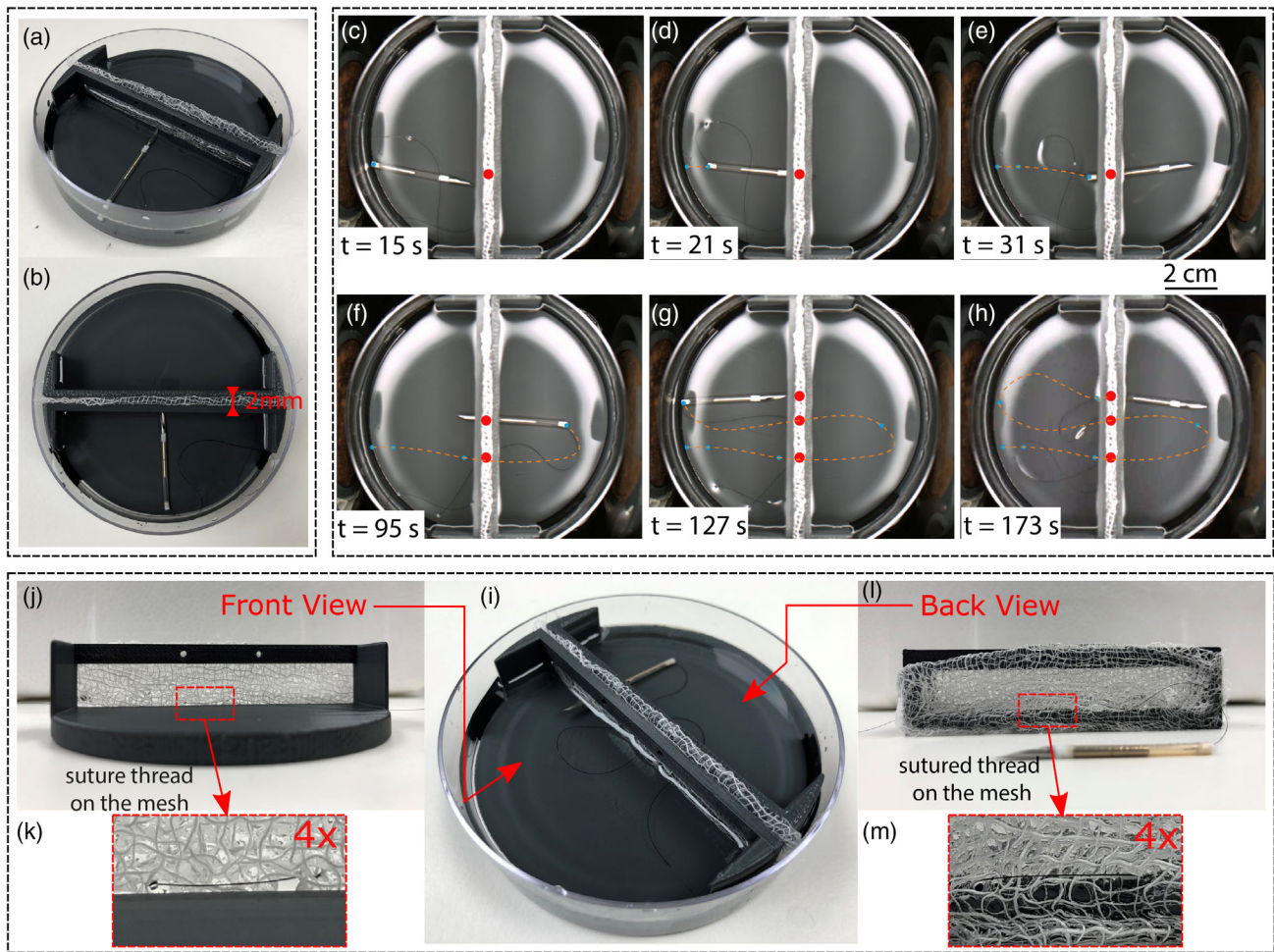


Figure 4. Suturing on agarose gel with a gauze mesh. a) The experimental setup for demonstrating the suturing capacity on an agar gel: we prepared a clamp mechanism that holds the sample and allows mobility for the suturing needle. b) The agar gel is 0.6% and 2 mm in thickness. A gauze mesh is covered around the agar gel to represent the meshes being used in hernia repair. c–h) The needle is being steered by a handheld remote controller in an open-loop fashion. An overhead camera is being used to provide real-time monitoring of the workspace. The needle has demonstrated three penetrations in less than 3 min. i–m) The suture thread used for suturing the mesh and the agar gel is shown after the completion of the suturing task. The suture thread used for the experiments is 50 μm thick.

We designed a 14 G hypodermic needle as the tip size of our MPACT-Needle for suturing demonstration. The MPACT-Needle for eye penetration implements a needle tip of 25 G, which is a clinically standard size for eye interventions. Even though such a size is capable of demonstrating the proof-of-concept manipulation and force advantage demonstrations of the impact mechanism, further miniaturization of the needle will be required for in vivo applications. With precise manufacturing techniques, the needle size can be reduced. Combining the miniaturized needle with a more powerful electromagnetic coil system will enable penetration of stiffer tissues via the application of stronger impact forces, enabling further needle miniaturization. In addition, more capable electromagnetic (EM) arrays will enable suturing via impact-based penetration action to be performed at farther distances, making use of larger workspaces. With appropriate power electronics, larger electromagnetic coils capable of generating cyclic impact-based forces at higher frequencies

(10–30 Hz range) could be designed and implemented, significantly expanding penetration possibilities. The relation between the ideal impact frequency versus electromagnetic coil power is provided in the Supplementary Information.

The tissue mass moving with the needle and the rigidity of the tissue mass could change the impact force delivered via the magnetic piston and the optimized duty cycle parameters. Even though the magnetic piston does not bounce back with the free-standing MPACT-Needle design, the tissue properties in contact with the needle may result in a bouncing-back behavior, resulting in differences in the impact force values and the optimized actuation sequence parameters. The mechanical responses vary from tissue to tissue, and determining the exact values would require a diligent set of simulation and characterization experiments related to the tissue properties and the needle–tissue interactions. We did not observe a critical difference in actuation sequence parameters in the demonstration

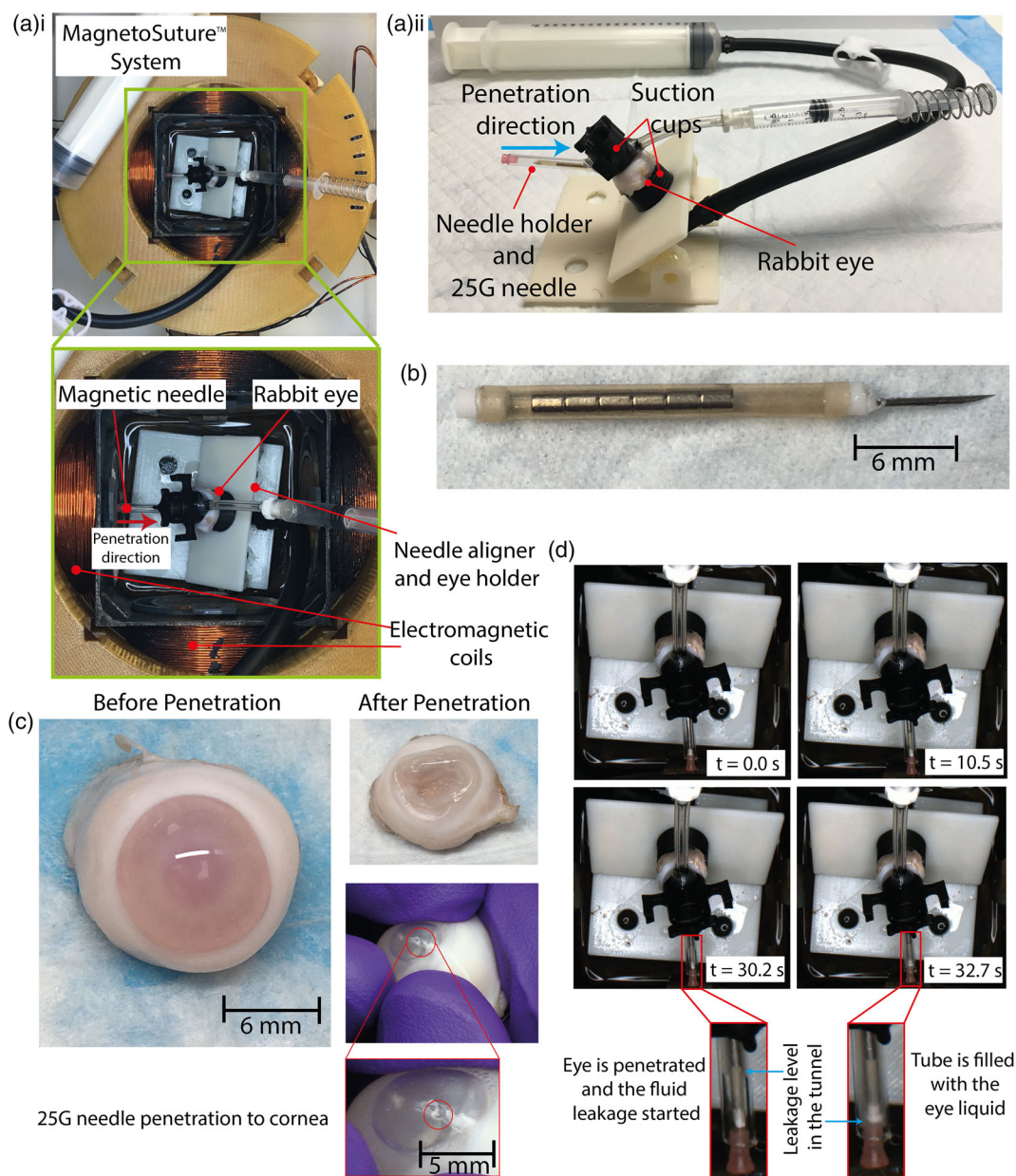


Figure 5. Eye penetration experiments. a) The holder structure used to stabilize the eye and mount the needle inside the coil system. b) The 25 G needle being used with the impact force mechanism. c) The experimental snapshots of the penetration video provided in Supplementary Video 2. The MPACT-Needle is able to puncture the eye in less than 30.1 s. d) Images of the rabbit eye before penetration and after penetration by the MPACT-Needle. Due to the puncturing deep in the eye, a passage from the cornea to the deeper tissue layers is opened. This passage allows for fluid exchange and delivering fluid drugs. We observe the leakage of the fluid from the inside of the eye toward the inside of the tube that holds the needle. A closer look reveals the location of penetration on the surface of the cornea.

experiments, but it could be more significant for stiffer and heavier tissue samples and it may require a further analysis on the tissue–needle dynamics.

We demonstrated our robot’s capability on a full-thickness transcorneal penetration scenario using a 25 G needle tip with a 14 G needle body. While standard 25 G needles are routinely used for full-thickness penetration tasks such as intravitreal injections, procedures that require partial thickness transcorneal penetration are more difficult for the surgeon to perform. Deep

anterior lamellar keratoplasty, for instance, requires a surgeon to place a 25 G needle within 60 μm of a tissue layer for a successful transplant.^[30] Perforation of this tissue layer is catastrophic to the surgery and despite microscope visualization, it occurs in up to 60% of cases for new surgeons.^[36] A magnetically controlled 25 G needle tip could be an ideal solution to achieve consistent and accurate partial tissue penetration of the cornea. Therefore, incorporating precise depth control would enable the MagnetoSuture System to complete more challenging surgical

tasks such as partial thickness corneal penetration for deep anterior lamellar keratoplasty. Depth control could be achieved by incorporating depth-sensing technology within the MPACT-Needle level. Modeling from our previous work, it would be feasible to embed an A-scan optical coherence tomography (OCT) fiber and use depth feedback control, to enable micrometer-level positioning of the MPACT-Needle in corneal tissue using the MagnetoSuture system as in the study by Opfermann et al.^[31] Therefore, future studies will aim to improve magnetic piston control over the impact pulse-based actuation with more precise timing of forward and backward motions throughout the entire workspace. Using the magnetic fields, the 1-DOF transcorneal penetration experiments can be improved to a 3-DOF penetration, similar to the magnetic suturing demonstration, for more complex interventional requirements to the cornea.

The penetration demonstrations are implemented in 2D planar surfaces (3-DOF) to show the proof of concept without introducing technical challenges of 3D (5-DOF) manipulation such as gravitational forces and lack of surface support. The capabilities shown in this study in 2D platforms can be applicable in 3D environments as well if the necessary hardware and setup is engineered. Adding a pair of z-coils and side-view cameras could be the minimum requirements to conduct 3D experiments for our system. The proposed robot design and impact mechanism would function similarly in 3D. As many clinically relevant scenarios are in 3D, adding a z-coil pair to magnetically actuate the robot for 3D penetration is an important future step to improve this novel magnetic device and come closer to clinical translation.

The level of autonomy proposed in this study is commanding the suturing needle via the user's handheld remote controller input. Therefore, the autonomy of the system can be represented as level 0 according to Yang et al.^[37] These handheld remote controller inputs can be used to rotate and translate the needles into desired poses with 3-DOF. Controlling the pulsing period for generating backward and forward cycles is implemented via user input as well. As the magnetic field strengths are highly nonlinear with respect to distance from the field source, such subcycles of pulling and pushing should be tuned depending on the location of the needle. In other words, K_b and K_f values should be tuned individually, depending on the distance of the magnet toward the pushing and pulling coils. Such tuning cannot be done manually in real-time steering. Extracting the robot position information and using this information to compute the K_b and K_f values that provide ideal functioning of the repetitive impact-force mechanism is a must. This would advance the autonomy of the system and allow better and smoother operation of the impact force mechanism. Improving the autonomy level would enable assistive interventional procedures and allow full automation of routine clinical procedures such as suturing. In the experiments, we have observed difficulty in exact positional control, particularly immediately after the needle completes a penetration. In such moments, the user's response is too slow to stop and prevent the needle from hitting the walls of the Petri dish. In a clinical scenario, this could introduce a safety issue. Therefore, a closed-loop control algorithm that can detect such sudden accelerations and prevent fatal movements is a must. Such autonomy can serve at an assistive level

to prevent user mistakes or to take responsibilities to conduct the tasks fully autonomously.

Assistive needle control techniques could be integrated, which could take the user input as the desired position and orientation for the needle and autonomously steer the needle into this desired position. A fully autonomous suturing needle would need to be capable of assessing and analyzing the overall suturing state. This requires advanced image processing algorithms as well as effective decision-making and needle steering strategies.^[38]

Finally, proper imaging methodologies for in vivo experiments should be integrated for autonomous tasks. Such imaging methodologies can consist of laparoscopic optical cameras, OCT, ultrasound, MRI, or X-ray fluoroscopy. While future efforts will expand on these results with further ex vivo and in vivo experiments, the work presented here establishes the physical parameters for tissue penetration using our MPACT-Needle and defines needed improvements with regard to image guidance and feedback. We envision that in vivo experiments would add additional challenges with respect to coordinate transformation, 3D localization, and localization challenges in dynamic and cluttered surgical environments.^[25] Focusing on the challenges related to 1) the safe and precise control of the impact mechanism in 3D environments; 2) intraoperative imaging for feedback to the surgeon and for autonomous control applications; and 3) in vivo demonstrations of the MPACT-Needle is the crucial next step to translate our studies into preclinical steps.

4. Experimental Section

Magnetic Actuation and Impact Dynamics: The magnetic pulling forces, F_m , and torques, T_m , acting on a magnetic body can be presented as

$$T_m = V_m(\mathbf{M}_m \times \mathbf{B}) \quad (5)$$

$$F_m = V_m(\mathbf{M}_m \cdot \nabla)\mathbf{B} \quad (6)$$

where V_m is the volume of the magnetic piston, \mathbf{M}_m is the average magnetization of the magnetic piston, and \mathbf{B} is the magnetic field vector generated by the electromagnetic coils. T_m allows rotation of the needle and pointing the needle tip in any desired direction. F_m provides the pulling force on the magnetic piston, causing the translation and impact momentum delivery inside the tube.

A basic Coulomb friction model indicates that the surface friction of the piston on the interior surface of the tube, F_f , is orders of magnitude smaller than the magnetic pulling force F_m . Therefore, for simplicity, we neglect the surface friction in our dynamics calculations. For the magnetic piston travelling from the tail to the tip of the needle on a planar surface under a constant average pulling force, F_m , Euler's law of rigid-body motion for the magnetic piston yields the equations of dynamics

$$F_{net} = ma = F_m + F_{impact} \quad (7)$$

where F_{net} is the net force on the magnetic piston. The impact force, F_{impact} occurs only when the piston hits the impact plate and can be computed as

$$F_{impact} = \begin{cases} f_{impact}(\mathbf{V}_{rel}), & \text{if } (||x_m|| \geq x_{crit}) \\ 0, & \text{otherwise} \end{cases} \quad (8)$$

where x_m is the center location of the magnetic piston, x_{crit} is the critical magnet center position where the contact to impact plate takes place, and \mathbf{V}_{rel} is the relative velocity between the magnetic piston and the impact plate. f_{impact} can be formulated by the simplified impact physics for two-rigid body collision with constant deceleration.^[39]

$$\mathbf{f}_{\text{impact}}(\mathbf{V}_{\text{rel}}) = -\frac{m\mathbf{V}_{\text{rel}}}{\Delta t_{\text{impact}}} \quad (9)$$

As shown in Equation (6), (7), and (8), there are two types of forces acting on the magnetic piston. While \mathbf{F}_m is the standard magnetic pulling force, $\mathbf{F}_{\text{impact}}$ occurs under the presence of contact with the impact plate.

The final force on the needle tip is the most important parameter for maximizing the penetration and suturing efficacy. For a needle penetrating into tissue, the environment-based torques and forces as well as magnetic forces and torques acting on the needle can be represented as

$$\mathbf{T}_{\text{needle}} = \mathbf{T}_m + \mathbf{T}_d \quad (10)$$

$$\mathbf{F}_{\text{needle}} = \begin{cases} \mathbf{F}_m - \mathbf{F}_{\text{impact}} + \mathbf{F}_d, & \text{if } (||x_m|| \geq x_{\text{crit}}) \\ \mathbf{F}_m + \mathbf{F}_d, & \text{otherwise} \end{cases} \quad (11)$$

External forces and torques due to the interactions with the environment or tissue are represented by \mathbf{F}_d and \mathbf{T}_d , respectively.

Impact-Based Actuation Mechanism: The impact-based actuation methodology requires an actuation sequence that pulls and pushes the magnetic piston back and forth along the direction of the penetration. The momentum accumulated on the piston travelling along the tubular structure is transferred to the impact plate in a short time, causing a much stronger momentary force. This sudden impact behavior provides a large penetration force on the magnetic needle that would not be achievable without a significant upgrade to the electromagnetic actuation hardware. This impact-based actuation mechanism is depicted in Figure 1b.

The back-and-forth motion of the magnet creates a certain sequence for the magnetic field and the gradient field applied. For a magnet penetrating along a desired direction \hat{r} , the applied magnetic field and gradient as a function of time should have the following properties

$$\mathbf{B}_m \parallel \hat{r} \quad (12)$$

$$\mathbf{F}_m(t) = \begin{cases} K_f ||\mathbf{F}_{\text{max}}|| \hat{r}, & \text{if } (\text{mod}(t, T) \geq D \cdot T) \\ -K_b ||\mathbf{F}_{\text{max}}|| \hat{r}, & \text{if } (\text{mod}(t, T) < D \cdot T) \end{cases} \quad (13)$$

where K_f and K_b are the forward and backward pulling force constants, respectively, limited between 0 and 1. \mathbf{B}_m is the magnetic field vector generated by the coils, \mathbf{F}_{max} is the maximum pulling force that is exerted on the magnet, t is the current time, T is the period duration for the full cycle of back-and-forth piston movement, and D is the duty ratio for the forward pulling duration limited between 0 and 1. This pulling force sequence over time with relevant parameters is depicted in Figure 2d.

In addition to the actuation parameters, the location of the needle has an important contribution. Because the magnetic field generated is not homogeneous within the workspace, that is, the field is stronger near to electromagnets, the backward pulling force and forward pulling force vary depending on the location of the magnet. If the needle is in line with the electromagnets and the tip is closer to the magnets than the tail, the forward pulling force is naturally stronger. In the opposite situation, where the tail of the needle is closer to the electromagnets, the backward pulling force dominates. Therefore, a handheld remote controller-based user input is continuously provided to tune D , K_f , and K_b such that the forward and backward travelling motion is satisfied throughout the entire workspace.

To characterize this impact behavior of the needle as a function of time-related parameters D and T , we created an experimental setup with a load cell (Transducer Techniques, GSO-1K) located inside of our magnetic system (Figure 3b). A 2D sweep along D and T was implemented. We swept the range from 0.2 to 0.8 with 0.1 increments for D and 50 to 250 ms with 50 ms increments for T . For each experiment, the impact motion lasted for 5 s, resulting in more than 20 cycles. The force readings are used to 1) compute the average impact force generated; and 2) compute the highest force density per time.

MagnetoSuture Setup: In this work, we implemented an optimized MPACT-Needle with the configuration shown in Figure 2. To demonstrate

the performance of the MPACT-Needle, we employed our physical MagnetoSuture system that was previously presented in the study by Mair^[33] and illustrated in Figure 1c. The needle was submerged in a viscous medium made by the water-glycerol mixture inside a Petri dish (diameter = 85 mm). The MPACT-Needle was tele-manipulated through external magnetic fields generated by an array of four uniformly spaced cylindrical electromagnets. Each electromagnetic coil was made by ≈ 12 wound layers of 54 turns of AWG 16 polyimide-coated copper wire ($N_{em} = 12 \times 54$). The inner diameter of the EM was 85 mm, their outer diameter was 98 mm (average diameter $2\rho_{em} = 91.5$ mm), and their length was $\ell_{em} = 60$ mm, as shown in Figure 1c. Four identical iron cores with diameters of 52.18 mm and lengths of 66.3 mm were inserted in the electromagnetic coils for boosting the magnetic field. The electromagnets are driven by two dual-channel H-bridge motor controllers (RoboClaw, Basic Micro Inc.) powered by an AC/DC converter capable of supplying 62.5 A and 48 VDC (PSE-3000-48-B, CUI Inc.). Visual feedback of the needle pose in the Petri dish was obtained using a FLIR Blackfly camera (BFS-U3-13Y3C-C) with a resolution of 1280×1024 pixels. The workspace was illuminated by a ring light mounted on a custom 3D-printed adapter.

Teleoperation System with a Handheld Remote Controller. The handheld remote controller (Xbox Controller, VOYEE) inputs were used to control the needle motion and its penetrating impulses teleoperatively. The user commands were implemented to rotate and translate the needle on a planar surface in real time while the operator monitored the needle via the top camera view. Moreover, the handheld remote controller input was used to apply the sequence of pulling and pushing the magnetic piston along this direction based on the parameters D , T , K_b , and K_f . It is important to have a changing value for K_b and K_f as the magnetic pulling forces were spatially nonlinear. While the needle changed its position, the ideal K_b and K_f constants should be updated. This tuning of constants was accomplished by the handheld remote controller's continuous buttons during the operation of the needle. Typically, K_b was kept in the range that provides the oscillatory hammering behavior while the net motion of the needle is forward.

Agar Gel Sample Preparation: Here, 0.6% agarose gel mimicking the stiffness of a brain tissue at 0.61 kPa elastic modulus^[40,41] with 3 mm thickness covered with a gauze mesh (CVS, Latex-free Gauze 5 CT) was used for the suturing experiment. A holder testbed, as shown in Figure 4, is designed. This testbed was aimed to clamp the samples perpendicularly to the planar needle workspace. Each testbed consisted of 1) two 3D-printed pieces which could form a circular horizontal platform (radius = 41 mm) and a standing clamping frame (height = 11 mm); 2) a Petri dish (inner radius = 43 mm); and 3) glycerin-water solution (30 mL) (Glycerin Vegetable, Sanco Industries, Inc., Fort Wayne, IN). The clamping frame was positioned at the center of the Petri dish. Hence, adequate space was left for steering the needle in the suture study. Depending on the thickness of the sample, a nonsticky tape was inserted between 3D-printed platform edges and Petri dish walls to close the gap and enhance the clamping functionality.

Rabbit Eye Experiment Preparation: Adult rabbit whole eyes were collected fresh in phosphate-buffered saline (PBS) with penicillin-streptomycin, amphotericin B, and gentamicin and shipped the same day on wet ice (The rabbit eyes were purchased by Pel-Freez Biologicals. As the animals were not euthanized by the vendor specifically for this study, the study was exempt from IACUC review and approval). Prior to testing, the rabbit eye was prepared by dissecting the conjunctiva and injecting PBS until the intraocular pressure was 20 mmHg. During experiments, the rabbit eye was placed in a whole eye holder (Figure 5a) and stabilized by applying vacuum using a 100 mL syringe. The whole eye holder was manufactured using a 12.7 mm NPT barbed hose fitting that was epoxied to a 3D-printed stand. The holder was designed to position the apex of the eye with the central axis of the MagnetoSuture System's coils.

The MPACT-Needle holder was manufactured by drilling a 0.5 mm hole at a 30° angle through the lateral wall of a corneal dissection trephine. A 2 mm-inner diameter polycarbonate round tube was cut to 50 mm length, aligned with the drilled hole, and epoxied to trephine. The size of the polycarbonate tube was chosen to accommodate the diameter of

the 25 G MPACT-Needle, while guiding the needle bevel to the apex of the rabbit cornea. After loading the 25 G MPACT-Needle, the polycarbonate tube was capped using an ABS plug. Prior to the experiments, the needle holder was manually aligned with the apex of the cornea and attached to the whole eye using a commercial trephine vacuum (Moria Surgical, 17202D800). A commercial trephine vacuum was used for all experiments so that the vacuum pressure did not exceed the clinical conditions. At the end of the experiment, the vacuum pressure was removed, releasing the trephine from the eye so that the MPACT-Needle penetration could be documented.

Force Characterization Measurements: A single-axis load cell (Transducer Techniques, GSO-1K) was located in the workspace of the MagnetoSuture setup. The voltage reading from the load cell's strain gauge was transferred to a data acquisition card (National Instruments, NI-9205) at a rate of 10 kS s^{-1} . Through the interface of a LabVIEW program, the voltage data was digitized and mapped into the force domain. Load cell characterization experiments showed that the measurements had the sensitivity of 5.69 mN. Prior to the force measurements, the tubular structure of the needle body was attached perpendicularly to the sensing region of the load cell using a cyanoacrylate-based adhesive.

To characterize the penetration forces in the agar gel phantom tissue with gauze and rabbit eye used in our experimental study, a needle penetration force recording system was setup using a syringe pump (PHD ULTRATM, Harvard Apparatus) as a linear motion stage (further details and illustration are available in Supplementary Information). The following force characterization experiments were performed.

Agar Gel with Gauze: A 14 G needle was attached to a single-axis load cell (Transducer Techniques, GSO-1K), which was fixed on the moving part of the syringe pump. A 3D-printed tissue holder was placed along the needle's moving direction. For enabling repeated needle penetration tests on the same piece of tissue sample, the location of the tissue holder was adjusted on the plane that was perpendicular to the needle's moving direction. We repeated the penetration on the same sample five times at various locations to generate penetration force ranges of both sample types. As a result of these experiments, we found out that the average penetration force of the agar gel with gauze was $248 \pm 98 \text{ mN}$.

Rabbit Whole Eye: Corneal penetration forces were measured by attaching a 25 G needle to the same single-axis load cell used in the agar penetration tests and mounting the system on the syringe pump. A whole rabbit eye holder was mounted at 30° with respect to the 25 G needle, and the linear stage was programmed to a velocity of 0.3 mm s^{-1} . Penetration forces were recorded until the needle advanced through the corneal tissue and into the intraocular space. The maximum penetration force was defined as the peak force during testing and the average peak penetration force was found to be $364.9 \pm 54.6 \text{ mN}$. Rabbit eyes were pressurized to 20 mmHg during all tests to minimize variance in the samples. Penetration forces for corneal tissue were measured on five samples and were reported as the average penetration force with associated standard deviation.

Statistical Analysis: The force characterization experiments for rabbit abdominal tissue penetration, agar gel penetration, and chicken breast tissue were repeated eight times ($n = 8$). Similarly, rabbit eye penetration and bacon strip penetration experiments were repeated five times ($n = 5$). The mean and standard deviation calculations were computed based on the highest point of force measured. The sampling rate of the data was 1 kHz.

Supporting Information

Supporting Information is available from the Wiley Online Library or from the author.

Acknowledgements

Authors thank Trevor Schwehr for paper reviewing and needle visualization, Wei-Hung Jung for his assistance on agarose gel preparation, and Matt Shaeffer for his guidance in high-speed camera usage. In addition,

research reported in this paper was supported by National Institute of Biomedical Imaging and Bioengineering of the National Institutes of Health under award number R01EB020610 and the National Eye Institute under award number R01EY032127. The content is solely the responsibility of the authors and does not necessarily represent the official views of the National Institutes of Health.

Conflict of Interest

The authors declare no conflict of interest.

Author Contributions

Conceptualization: O.E., X.L., L.O.M., I.N.W., J.U.K., W.G., Y.D.M., A.K.; Methodology: O.E., X.L., J.G., J.O., L.O.M., Y.B., A.K.; Software: O.E., Y.B., J.O.; Visualization: O.E., J.G.; Data Curation: O.E.; Optimization Study: O.E.; Needle Manufacturing: O.E., L.O.M.; Experiments: O.E., X.L., J.G., J.O.; Funding acquisition: A.K.; Supervision: Y.D.M., A.K.; Writing – original draft: O.E., X.L., J.G., J.O., Y.B., L.O.M., A.K.; Writing – review & editing: O.E., X.L., J.G., J.O., L.O.M., J.U.K., W.G., Y.D.M., A.K.

Data Availability Statement

The data that support the findings of this study are available in the supplementary material of this article.

Keywords

magnetic systems, medical robotics, miniature robotics, surgical robots, tissue penetration

Received: March 24, 2022
Published online: April 22, 2022

- [1] S. Maeso, M. Reza, J. A. Mayol, J. A. Blasco, M. Guerra, E. Andradás, M. N. Plana, *Ann. Surg.* **2010**, *252*, 254.
- [2] J. J. Abbott, E. Diller, A. J. Petruska, *Annu. Rev. Control Rob. Auton. Syst.* **2020**, *3*, 57.
- [3] O. Erin, H. B. Gilbert, A. F. Tabak, M. Sitti, *IEEE Trans. Rob.* **2019**, *35*, 1323.
- [4] M. P. Kummer, J. J. Abbott, B. E. Kratochvil, R. Borer, A. Sengul, B. J. Nelson, *IEEE Trans. Rob.* **2010**, *26*, 1006.
- [5] S. Martel, J.-B. Mathieu, O. Felfoul, A. Chanu, E. Aboussouan, S. Tamaz, P. Pouponneau, L. Yahia, G. Beaudoin, G. Soulez, M. Mankiewicz, *Appl. Phys. Lett.* **2007**, *90*, 114105.
- [6] O. Erin, J. Giltinan, L. Tsai, M. Sitti, in *2017 IEEE Inter. Conf. on Robotics and Automation (ICRA)*, IEEE, Singapore, Singapore **2017**, pp. 3404–3410.
- [7] B. J. Nelson, I. K. Kaliakatsos, J. J. Abbott, *Annu. Rev. Biomed. Eng.* **2010**, *12*, 55.
- [8] X.-Z. Chen, B. Jang, D. Ahmed, C. Hu, C. De Marco, M. Hoop, F. Mushtaq, B. J. Nelson, S. Pané, *Adv. Mater.* **2018**, *30*, 1705061.
- [9] M. Sitti, H. Ceylan, W. Hu, J. Giltinan, M. Turan, S. Yim, E. D. Diller, in *Proc. IEEE* **2015**, *103*, 205.
- [10] N. Simaan, R. M. Yasin, L. Wang, *Annu. Rev. Control Rob. Auton. Syst.* **2018**, *1*, 465.
- [11] M. N. Huda, H. Yu, S. Cang, *Rob. Comput. Integr. Manuf.* **2016**, *41*, 127.
- [12] A. W. Mahoney, J. J. Abbott, *Int. J. Rob. Res.* **2016**, *35*, 129.
- [13] G. Ciuti, P. Valdastrì, A. Menciassi, P. Dario, *Robotica* **2010**, *28*, 199.

- [14] F. Carpi, N. Kastelein, M. Talcott, C. Pappone, *IEEE Trans. Biomed. Eng.* **2010**, *58*, 231.
- [15] S. Yim, M. Sitti, *IEEE Trans. Rob.* **2011**, *28*, 183.
- [16] D. Son, H. Gilbert, M. Sitti, *Soft Rob.* **2020**, *7*, 10.
- [17] T. Kobayashi, M. Ochi, S. Yanada, M. Ishikawa, N. Adachi, M. Deie, K. Arihiro, *Arthrosc. - J. Arthrosc. Relat. Surg.* **2008**, *24*, 69.
- [18] J. Leclerc, B. Isichei, A. T. Becker, *IEEE Rob. Autom. Lett.* **2018**, *3*, 4367.
- [19] J. Rahmer, C. Stehning, B. Gleich, *PLoS One* **2018**, *13*, e0193546.
- [20] S. Yim, E. Gultepe, D. H. Gracias, M. Sitti, *IEEE Trans. Biomed. Eng.* **2013**, *61*, 513.
- [21] P. Vartholomeos, C. Bergeles, L. Qin, P. E. Dupont, *Int. J. Rob. Res.* **2013**, *32*, 1536.
- [22] M. Li, Y. Tang, R. H. Soon, B. Dong, W. Hu, M. Sitti, *Sci. Adv.* **2022**, *8*, 10eabm5616.
- [23] D. Son, M. C. Ugurlu, M. Sitti, *Sci. Adv.* **2021**, *7*, eabi8932.
- [24] L. Yan, Y. Liu, L. Zhang, Z. Jiao, C. Gerada, *IEEE Trans. Ind. Electron.* **2018**, *66*, 9112.
- [25] W. Pryor, Y. Barnoy, S. Raval, X. Liu, L. Mair, D. Lerner, O. Erin, G. D. Hager, Y. Diaz-Mercado, A. Krieger (Preprint) *arXiv:2105.09481, v1, submitted: May 2021*.
- [26] A. T. Becker, O. Felfoul, P. E. Dupont, in *2015 IEEE Inter. Conf. on Robotics and Automation (ICRA)*, IEEE, Seattle, WA **2015**, pp. 1184–1189.
- [27] J. Leclerc, A. Ramakrishnan, N. V. Tsekos, A. T. Becker, *IEEE Rob. Autom. Lett.* **2017**, *3*, 403.
- [28] A. Quelin, L. Petit, C. Prella, N. Damay, in *2021 IEEE Inter. Conf. on Mechatronics (ICM)*, IEEE, Kashiwa Japan **2021**, pp. 1–6.
- [29] O. Erin, M. Boyvat, M. E. Tiryaki, M. Phelan, M. Sitti, *Adv. Intell. Syst.* **2020**, *2*, 1900110.
- [30] W. J. Reinhart, D. C. Musch, D. S. Jacobs, W. B. Lee, S. C. Kaufman, R. M. Shtein, *Ophthalmology* **2011**, *118*, 209.
- [31] J. Opfermann, M. Barbic, M. Khrenov, S. Guo, N. Sarfaraz, J. Kang, A. Krieger, in *2021 IEEE/RSJ Inter. Conf. on Intelligent Robots and Systems (IROS)*, IEEE, Prague, Czech Republic **2021**, pp. 757–764.
- [32] F. Pervin, W. W. Chen, *Dynamic Behavior of Materials*, Vol. 1, Springer, New York, NY **2011**, pp. 9–13.
- [33] L. O. Mair, X. Liu, B. Dandamudi, K. Jain, S. Chowdhury, J. Weed, Y. Diaz-Mercado, I. N. Weinberg, A. Krieger, *IEEE Trans. Med. Rob. Bionics* **2020**, *2*, 206.
- [34] A. Matthews, C. Hutnik, K. Hill, T. Newson, T. Chan, G. Campbell, *Eye* **2014**, *28*, 880.
- [35] A. C. Gonçalves, S. Cavassana, F. R. Chavarette, R. Outa, S. J. Casarin, A. V. Corazza, *J. Healthcare Eng.* **2020**, *2020*, 1.
- [36] M. Ünal, B. Bilgin, I. Yucel, Y. Akar, C. Apaydin, *Ophthalmic Surg. Lasers Imaging Retina* **2010**, *41*, 642.
- [37] G.-Z. Yang, J. Cambias, K. Cleary, E. Daimler, J. Drake, P. E. Dupont, N. Hata, P. Kazanzides, S. Martel, R. V. Patel, V. J. Santos, R. H. Taylor, *Sci. Rob.* **2017**, *2*, 8638.
- [38] G.-Z. Yang, J. Bellingham, P. E. Dupont, P. Fischer, L. Floridi, R. Full, N. Jacobstein, V. Kumar, M. Mcnutt, R. Merrifield, B. J. Nelson, B. Scassellati, M. Taddeo, R. Taylor, M. Veloso, Z. L. Wang, R. Wood, *Sci. Rob.* **2018**, *3*, eaar7650.
- [39] D. Z. Yankelevsky, V. R. Feldgun, *Int. J. Prot. Struct.* **2020**, *11*, 515.
- [40] S. Shahab, M. Kasra, A. Dolatshahi-Pirouz, *Plos One* **2021**, *16*, e0247727.
- [41] A. Gefen, S. S. Margulies, *J. Biomech.* **2004**, *37*, 1339.